Available online at www.sciencedirect.com

ScienceDirect

Acta Materialia 86 (2015) 182–192

Acta MATERIALIA

www.elsevier.com/locate/actamat

Grain boundary segregation engineering and austenite reversion turn embrittlement into toughness: Example of a 9 wt.% medium Mn steel

Margarita Kuzmina, Dirk Ponge* and Dierk Raabe

Max-Planck Institut für Eisenforschung GmbH, Max-Planck Straße 1, 40237 Düsseldorf, Germany

Received 30 October 2014; revised 2 December 2014; accepted 9 December 2014

Abstract—We study grain boundary embrittlement in a quenched and tempered Fe–Mn high-purity model martensite alloy using Charpy impact tests and grain boundary characterization by atom probe tomography. We observe that solute Mn directly embrittles martensite grain boundaries while reversion of martensite to austenite at high-angle grain boundaries cleans the interfaces from solute Mn by partitioning the Mn into the newly formed austenite, hence restoring impact toughness. Microalloying with B improves the impact toughness in the quenched state and delays temper embrittlement at 450 °C. Tempering at 600 °C for 1 min significantly improves the impact toughness and further tempering at lower temperature does not cause the embrittlement to return. At higher temperatures, regular austenite nucleation and growth takes place, whereas at lower temperature, Mn directly promotes its growth.

Keywords: Medium Fe–Mn alloy; Embrittlement; Grain boundary segregation; 3-D atom probe tomography; Austenite reversion

1. Introduction

From a thermodynamic standpoint, Fe–Ni alloys [1–4] can be replaced by the less expensive Fe–Mn alloys. They lead to very similar microstructures, e.g., lath martensite and mechanical properties that are similar to those of Fe–Ni alloys. However, ferritic Fe–Mn alloys tend to undergo strong embrittlement at low temperatures [1]. Among the possible explanations for the embrittlement in medium Mn alloys, the segregation of both P and N [2] or N alone [5] have been suggested to reduce grain boundary cohesion. Bolton et al. [6] speculated that the Mn/Si ratio controls the susceptibility to temper embrittlement. In their study, however, the role of N and C remained unclear. It has been observed that the addition of Mn shifts the ductile to brittle transition temperature (DBTT) towards higher temperatures [7]. It was assumed that the higher Mn content enhanced the effect of harmful impurities [6,8]. Different solutions were suggested to lower the DBTT in medium Mn steels, e.g. by microalloying with Mo [6] or B [9], the introduction of stable austenite [4,10] or grain refinement [3]. Although the mechanical properties were indeed improved in most of these approaches, medium Fe–Mn steels cannot be used at liquid nitrogen temperature [4]. Hence, they are not suited for structural applications at very low temperatures.

Recently, medium Mn steels (3–12%) have received much attention as third-generation high-strength steels [11–13] owing to their excellent mechanical properties. Adding 1–3 wt.% Ni and Al promotes precipitation hardening in the martensite matrix [14,15]. The minor addition of C (up to 0.2 wt.%) improves the austenite reversion kinetics and austenite stability, and increases the strength of the alloy [12]. In this context, there is a need to better understand tempering embrittlement in the Fe–Mn system. Nasim et al. recently [8] proposed that segregation of Mn, N and P to grain boundaries is the main cause for the embrittlement, but later admitted that the segregation of Mn alone, i.e., even in the absence of N and P, could be a possible reason for embrittlement too [16]. Heo et al. [17] performed auger electron spectroscopy (AES) measurements on an embrittled surface of an Fe–12 wt.% Mn alloy and attributed this to a direct solute embrittling effect caused by Mn, but the surprising effect of toughness retrieval at 400 °C at longer annealing times was not studied. Using a Yoffee diagram, Kwon et al. [18] explained the intergranular fracture of Fe–8 wt.% Mn in the quenched state in terms of a higher matrix strength compared to the cohesion of the grain boundaries, which they probed by nanohardness. However, when adding 40 ppm C to Fe–8 wt.% Mn, intergranular fracture is not observed even at −196 °C, despite the lower hardness of the grain boundary region compared to that of the matrix. Also, no analysis of material in the as-tempered state was conducted, and it is unclear whether the relative difference between

* Corresponding author. Tel.: +49 211 6792 960; fax: +49 211 6792 333; e-mail: d.ponge@mpie.de

http://dx.doi.org/10.1016/j.actamat.2014.12.021
1359-6462/

the matrix and grain boundary hardnesses would further increase with tempering time.

In order to utilize Mn segregation [17] for grain boundary engineering [19], a better understanding of the underlying mechanisms that lead to grain boundary embrittlement is required. Atom probe tomography (APT), with its capability of 3-D analytical mapping of materials at atomic-scale resolution and with ppm detection sensitivity for all elements [20–22], is an ideal tool with which to quantitatively study grain boundary segregation, even in the initial stage of tempering. Thus, the goal of this work was to quantify grain boundary segregation in Fe–9 wt.% Mn by applying APT to gain a better understanding of the atomistic mechanisms of both solute Mn-driven grain boundary embrittlement and the opposite trend promoted by martensite-to-austenite reversion at interfaces.

2. Experiments

2.1. Materials and methods

A nominal model composition of 9 wt.% Mn (Mn9) was chosen to ensure complete formation of lath martensite upon quenching in water or oil. The impurity content was reduced to a negligible level to eliminate the influence of any elements other than Mn. The addition of 30 ppm B in the second model alloy Mn9+B was done to ensure the suppression of a P-induced temper embrittlement [9,23,24] and additionally to enhance grain boundary cohesion [25]. At the same time, in order to prevent the precipitation of boron nitrides, 0.05 wt.% of Ti and Al were added to the alloy, as these elements have a high affinity to nitrogen. Table 1 summarizes the bulk chemical compositions after homogenization according to wet chemical analysis.

Alloys Mn9 and Mn9+B were cast into rectangular billets of 4 kg each in a vacuum induction furnace. The slabs were hot rolled at 1100 °C from 60 to 6 mm thickness and then water quenched. Subsequently, the edges of the slab were trimmed to avoid any influence of macrosegregations. The billets were reheated to 1100 °C for 1 h for homogenization, i.e., to minimize the segregation banding of Mn. Alloy Mn9 was then water quenched while Mn9+B was oil quenched to ensure B segregation to grain boundaries during cooling. Final heat treatment was conducted at different temperatures between 400 and 600 °C (in a two-phase region ($\alpha+\gamma$)) for a period between 10 s and 860 h, and then water quenched. Short heat treatments were performed in a liquid tin bath. Long heat treatments (more than 10 min) were performed in an air-circulated furnace.

Charpy impact tests were performed on longitudinal subsized Charpy V notch specimens with dimensions of $3 \times 4 \times 27$ mm^3, with a 60° notch perpendicular to the rolling plane according to EN-10045. The accurate temperature of the sample during the test was assured by a welded thermocouple.

Atomic-scale composition analysis of grain boundaries after tempering was conducted using APT. Electron backscattered diffraction (EBSD) analysis was employed to identify prior austenite grain boundaries (PAGBs) with non-special misorientation, i.e., avoiding low Σ coincidence site lattice boundaries. Samples were prepared for APT by focused ion beam (FIB) milling in a FEI Helios NanoLab600i. With this site-specific preparation method, grain boundaries were prepared parallel to the analysis direction of the tip. The sample preparation route is summarized in Fig. 1. Samples were mounted on a pre-fabricated Si microtip array. Subsequently, annular milling was used to shape the posts into the form of sharp tips with radii of <100 nm.

APT characterization was conducted on a LEAP 3000X HR instrument (Cameca) at a base temperature of 50 ± 4 K, operated in laser-pulsed mode (wavelength 532 nm; pulse repetition rate: 250 kHz) with 0.4 nJ pulse energy. Reconstruction was carried out using the commercial software Cameca IVAS® following the protocol introduced by Geiser et al. [26].

3. Experimental results

3.1. Mechanical properties

In the as-quenched condition, the hardnesses of alloys Mn9 and Mn9+B are 288±3HV5 and 288±8HV5 and the

Table 1. Chemical compositions of the two high-purity model alloys Mn9 and Mn9+B.

Alloy	wt.%	wt. ppm										
	Mn	C	Ni	Mo	Ti	Si	Al	S	P	O	N	B
Mn9	9.04	49	<10	<20	<10	24	<20	24	<20	250	35	<10
Mn9+B	8.80	85	580	47	338	61	331	44	<20	24	20	27

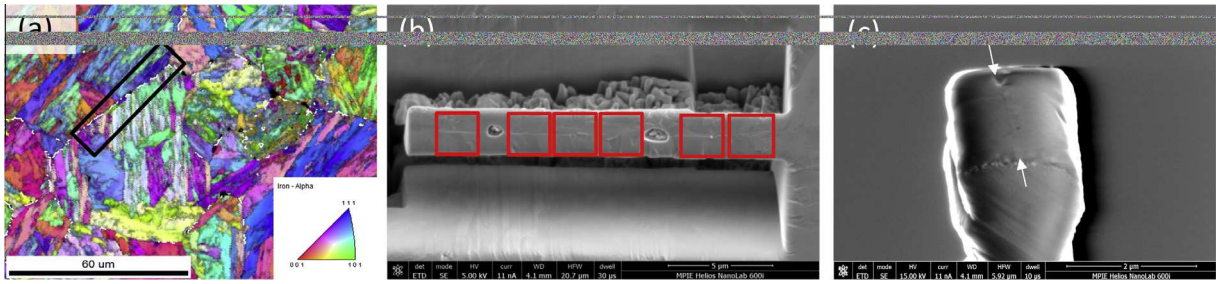

Fig. 1. Site-specific APT preparation of a PAGB. (a) EBSD scan with a marked PAGB; (b) SEM image of an FIB-milled grain boundary, containing six tips; (c) configuration before an annular milling of the tip.

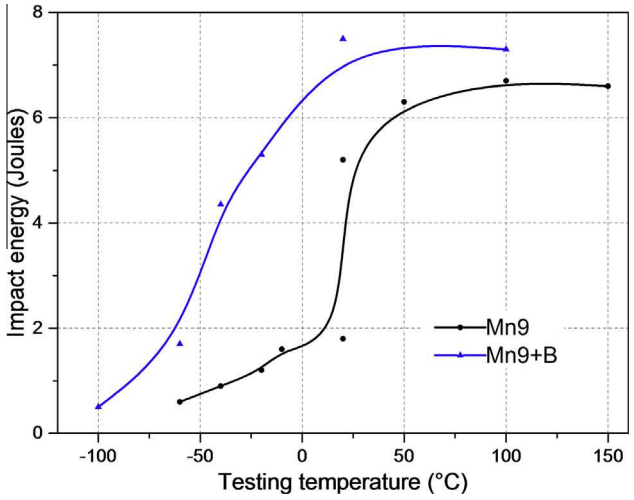

Fig. 2. DBTT curves of high-purity Mn9 and Mn9+B.

prior austenite grain sizes are 50 and 30 μm, respectively. The DBTT was calculated as the temperature of half of the sum of the upper and lower shelf energies. A DBTT of 20 °C was determined for the as-quenched alloy Mn9. The addition of B improved the energy of the upper shelf and shifted the DBTT to −40 °C (Fig. 2). For a better comparison of impact toughness values among the Mn9 and Mn9+B alloys, and to confine the number of experiments further, impact toughness tests were conducted at room temperature for both alloys.

The impact toughness of Mn9 tempered at 450 and 600 °C is shown in Fig. 3a. It has already dropped at both tempering temperatures by 10 s. During this short tempering exposure the fracture mode changed from mixed intercrystalline-ductile in the quenched state (Fig. 4a) to a fully intergranular failure after tempering at 450 °C (Fig. 4b). The PAGBs become the weakest crack propagation path in the microstructure. The impact toughness curve of Mn9 in Fig. 3a shows a convex profile with an unexpected increase after longer holding times, i.e., 30 s at 600 °C and 672 h at 450 °C. An examination of the fracture surface after 672 h at 450 °C revealed a small fraction of ductile dimples next to intergranular facets. Upon careful analysis of the intergranular failure after a long holding time, we observe that the grain boundaries have a microdimpled structure, which is known as pseudo-intercrystalline brittleness [27]. After 3 min of tempering at 600 °C, the fracture mode is predominantly ductile (Fig. 4d), with a small fraction of brittle intercrystalline fracture in the center of the fractured surface, where a triaxial stress state prevails.

Alloy Mn9+B displays impact properties which are similar to those of Mn9. After tempering at 450 °C, we observe a decrease in impact toughness, which is, however, delayed in comparison to Mn9.

The hardness results of Mn9 in Fig. 3b reveal an instantaneous decrease in hardness at 600 °C and a slow decrease, followed by a small increase in the beginning of tempering at 450 °C. The slight increase in hardness in both samples Mn9 and Mn9+B (Fig. 3d) has been earlier attributed to the formation of MnN, as suggested by Nasim et al. [8]. However, no MnN was observed in any of our measurements. As an underlying reason for this effect could be the static strain aging we observed by the segregation of Mn to dislocations, as will be reported elsewhere [28].

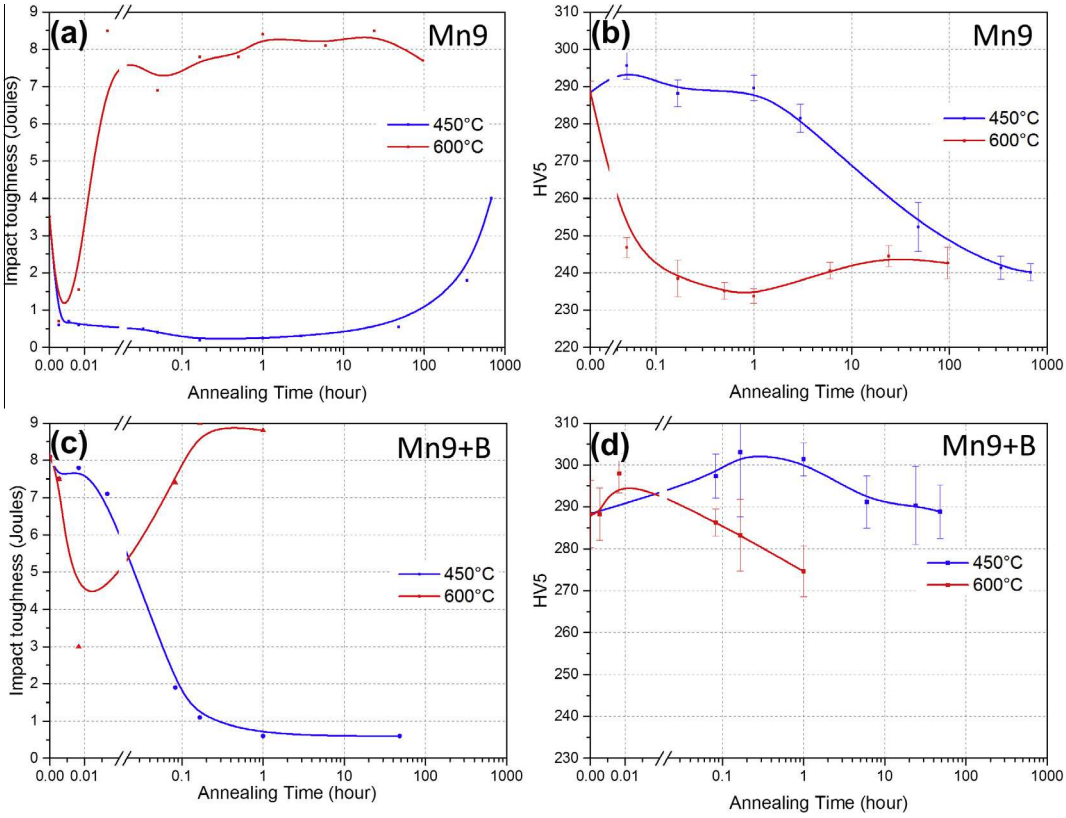

Fig. 3. Influence of annealing time and temperature on (a) room-temperature impact toughness of alloy Mn9; (b) hardness of Mn9; (c) room-temperature impact toughness of a tempered Mn9+B; (d) hardness of Mn9+B.

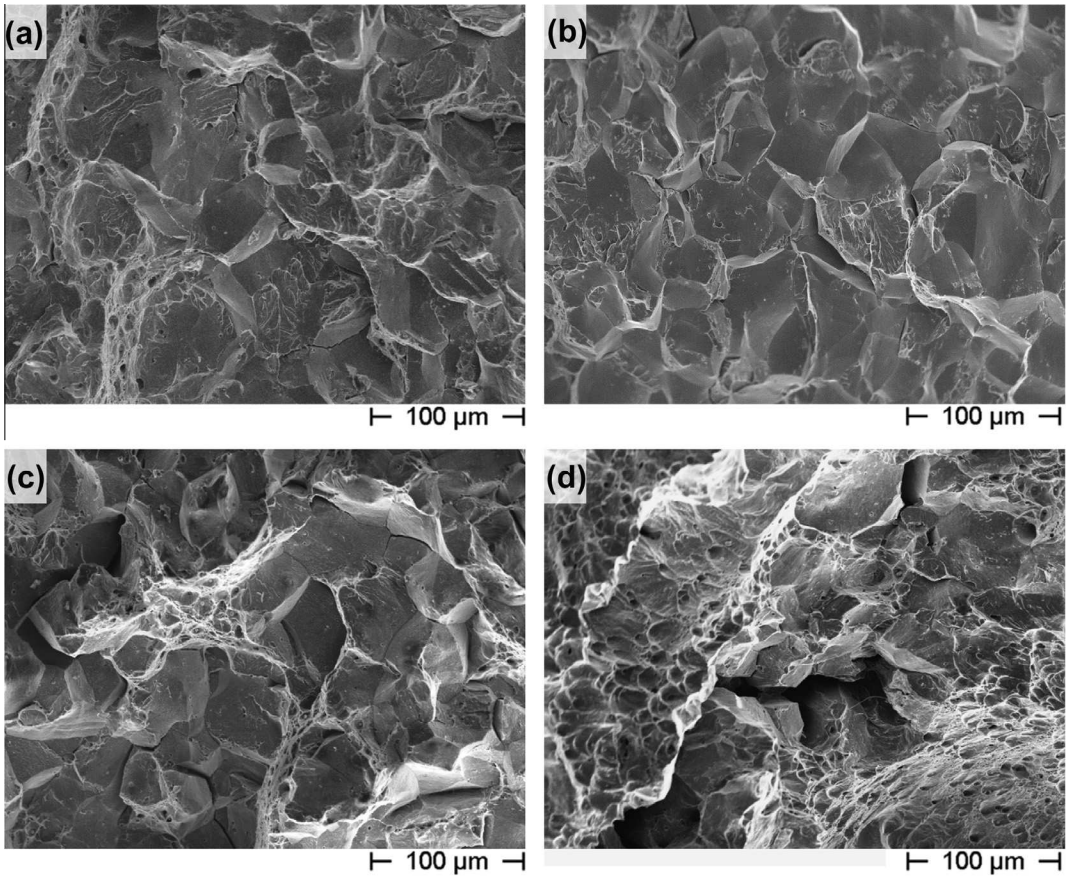

Fig. 4. Scanning electron micrograph of fracture surfaces of Mn9, fractured at 25 °C. (a) Quenched state; (b) after annealing at 450 °C for 10 s; (c) after annealing at 450 °C for 672 h with a magnified image; (d) after annealing at 600 °C for 3 min.

The effect of material strength on fracture properties is summarized by the Yoffee diagram [29,30], which states that when the peak stress at the crack tip reaches the yield stress first, the fracture is ductile. If the brittle fracture stress is reached before the yield stress, then the crack propagates in brittle mode. To understand the correlation between the hardness and the return of the toughness for sample Mn9, for instance after long annealing times at 450 °C, a series of heat treatments in the temperature range 400–600 °C was conducted. The tempering time for sample Mn9 was chosen in such a way as to keep the Mn diffusion distance constant at a level of 37 nm for all the cases. The resulting "equal diffusion range" tempering times vary from 4 min at 600 °C to 860 h at 400 °C. The resulting variations in hardness and impact toughness are shown in Fig. 5. After all tempering treatments, the hardness values remain constant, but the toughness changes as a function of temperature, with a DBTT of around 540 °C. This gives us a strong indication that in a medium Mn alloy the reversion of toughness at 450 and 600 °C is not primarily connected to the material hardness but instead to another diffusion-driven toughness recovery mechanism.

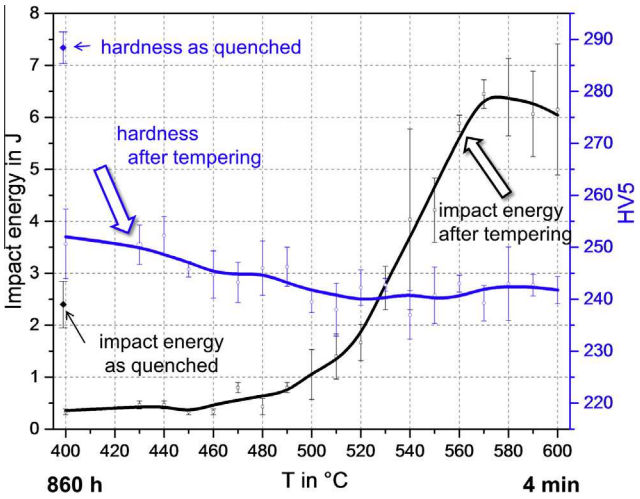

Fig. 5. Impact energy and hardness of the model alloy Mn9 plotted as a function of annealing temperature. The annealing time (ranging from 860 h for 400 °C to 4 min at 600 °C) was adjusted to ensure the same diffusion length for Mn (37 nm) for all the heat treatments.

3.2. APT results

Besides hardening embrittlement [31,32], a decrease in grain boundary cohesion caused by segregation [33] of harmful impurities is a possible reason for intergranular embrittlement. In order to differentiate between the two mechanisms, APT was performed on PAGBs in both of the model alloys, Mn9 and Mn9+B, in the as-quenched state and after tempering for different times at 450 and 600 °C. Several grain boundaries were probed for each sample condition. Some insignificant variations in composition were observed among measurements conducted in the same tempering state. Compositional variations along one

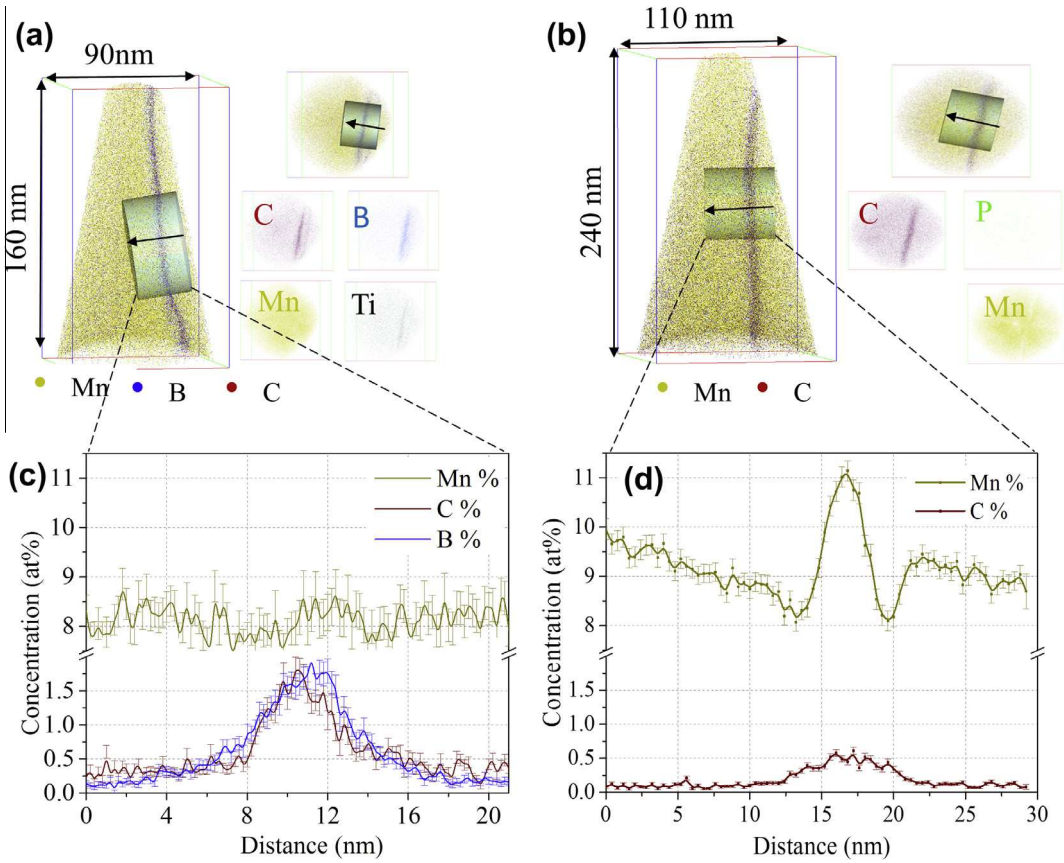

Fig. 6. (a) APT results of Mn9+B in the as-quenched state. Top and side views of the dataset, with the corresponding element distribution maps revealing the accumulation of C, B and Ti on the PAGB and a homogeneous distribution of Mn, P and N. A corresponding 1-D concentration profile along the cylindrical unit (c) shows the homogeneous distribution of Mn and the enrichment of C and B; (b) APT results obtained on Mn9 tempered at 450 °C for 1 min. 3-D side view and top view of the dataset of the same region, with the corresponding element distribution maps revealing the accumulation of C and Mn on the PAGB and the homogeneous distribution of P; a corresponding 1-D concentration profile along the cylindrical unit is shown in (d).

grain boundary have been revealed before, by Miller and Yao [34], Krakauer and Seidman [35] and Herbig et al. [36]. In the present study, therefore, average Gibbsian interfacial excesses values are presented.

In the as-quenched state in the Mn9+B alloy, no evidence was obtained for segregation of any harmful elements (P, Sn, Sb, Si, As, N or O). A typical dataset is shown in Fig. 6a. In this case, segregation of B and Ti occurred during slow cooling after homogenization heat treatment. When probing the composition across the grain boundary, we detected no segregation of Mn. In the alloy Mn9 in the as-quenched state, no segregation of Mn or P is expected because the material was immediately water quenched from austenite. This result is in agreement with an AES measurement of Nasim et al. [8] and the APT measurements of Kwon et al. [18].

After tempering at 450 °C for 1 min, the alloy Mn9 becomes brittle, revealing a fracture path along the PAGBs. The ion distribution maps in Fig. 6b show slight segregation of C and B to the grain boundary. No segregation of P or any other harmful element was found. The absence of N segregation to the grain boundary confirms that this effect cannot be the cause for grain boundary embrittlement in the as-quenched state, as was considered in Refs. [5,8]. Fig. 6d shows enrichment of Mn at the grain boundary of up to 11 at.% in the form of a 1-D concentration profile.

Fig. 7a and b shows concentration profiles across PAGBs in Mn9+B after tempering for 10 and 60 min, respectively. An increase in Mn and decrease in B segregation levels is also observed.

Alloy Mn9 was tempered further for an extended period of time. With increasing holding time at 450 °C the Mn concentration on the PAGB increases and reaches ~18 at.% Mn after 48 h. However, surprisingly, after 336 h tempering at 450 °C, the grain boundary concentration strongly decreased to a value of only 8 at.% Mn. Fig. 8a provides an ion map containing a grain boundary (top) together with a concentration profile across the grain boundary (bottom). We observe that the concentrations of Mn and C on the grain boundary have decreased, while that of P has not changed. Fig. 8b reveals a Mn-rich phase (austenite) at a grain boundary. C is enriched inside this phase and P is pushed out of it onto the phase boundary, which can be explained by the lower solubility of P in austenite than in ferrite.

After 336 h, the possible martensite-to austenite reversion islands are suppossed to be too small to be detected by high resolution EBSD. After 672 h of tempering, the two-phase structure consisting of relaxed martensite and reversed austenite evolves further and can be mapped by EBSD, as shown in Fig. 9. Austenite islands preferentially nucleate at triple junctions, intersections of lath and

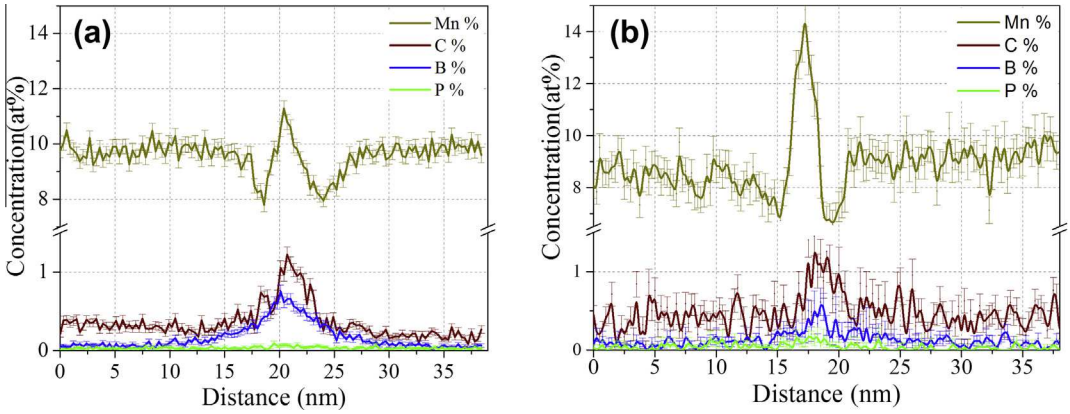

Fig. 7. Grain boundary concentration profiles in Mn9+B: (a) after tempering at 450 °C for 10 min; (b) after tempering at 450 °C for 1 h.

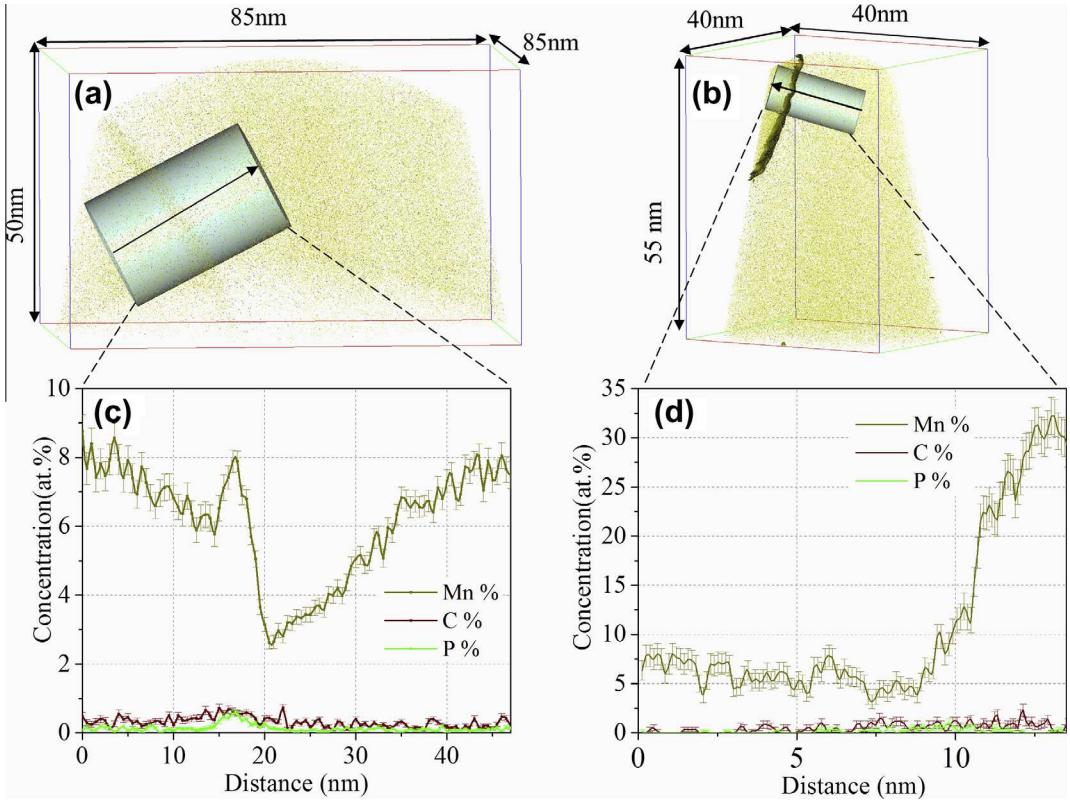

Fig. 8. Mn9 at 450 °C after 336 h. (a) PAGB and corresponding 1-D concentration profile (c) across the GB. It is enriched with Mn, C and P; (b) Mn-rich phase and corresponding 1-D concentration profile (d) across the austenite reversion zone. Enrichment of up to 32 at.% Mn and 0.7 at.% C are observed. A small enrichment of P is found at the phase boundary.

high-angle grain boundaries, and at PAGBs, as has been observed for Fe–Mn [37,38] and Fe–C [39–41].

Table 2 displays absolute grain boundary concentrations and excess values of Mn, C, B and P for different tempering states for both the model alloys Mn9 and Mn9+B. Fig. 10 summarizes grain boundary excess values for Mn9 and Mn9+B for better visual comparison. Absolute concentrations are easier to understand, but they do not necessarily reflect thermodynamic mechanisms and do not contain changing matrix compositions. An excess value averages the grain boundary composition and is independent of APT reconstruction and evaporation artifacts [20]. Local magnification effects are examples of such effects: these are visible, for example, in Fig. 11b, in terms of the broad apparent lateral extension of the segregation or in the form of a segregation asymmetry such as observed in Fig. 8. Values of interfacial excesses were calculated according to the method of Krakauer and Seidman [35]. Differences in segregation level depend on the grain boundary type and misorientation angle [36,42,43]. Here, only PAGBs with random misorientation were investigated to minimize the influence of the misorientation effect.

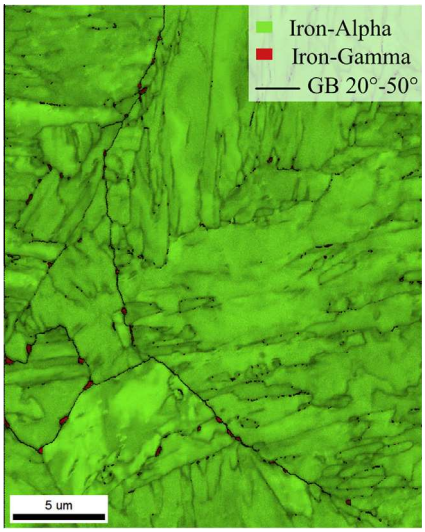

Fig. 9. EBSD phase map of model alloy Mn9 after tempering at 450 °C for 672 h. Very small austenite regions decorate triple points, PAGBs and high-angle grain boundaries.

4. Discussion

4.1. Grain boundary segregation and embrittlement

After tempering at 450 °C for 1 min, the embrittled grain boundaries in the model alloy Mn9 are enriched with C (1.1 atoms nm^{-2}) and Mn (4.8 atoms nm^{-2} excess). This observation indicates that one of these two elements or their combination promotes grain boundary decohesion. We should underline that no As, Sb, O, N or P enrichments were found on the embrittled grain boundaries, at least after 1 min of tempering at 450 °C. For comparison, Duchateau and Guttmann [10] detected P segregation in microduplex 6–9% Mn steels by AES and claimed that it was a reason for embrittlement. In our alloy no P segregation was detected due to its ultralow nominal content, i.e., our material contains less than 20 ppm, in comparison to the 30 ppm P in the material probed by Duchateau and Guttmann [10]. The effect of C on grain boundary cohesion is generally believed to be positive, as has been theoretically shown by Wu et al. [44] and Seah [45]. Also, enrichment of C was observed at the grain boundary in Mn9 after tempering for 10 min at 600 °C. In this state the alloy was not brittle, thus we conclude that there is no negative effect of C on impact toughness. In contrast, recent studies on the effect of Mn on grain boundary strength in Fe reveal that Mn can lead to direct embrittlement [46,47]. The experimental results of Nikbakht et al. [16] and Heo et al. [17] also showed Mn segregation to grain boundaries in a binary medium Mn steel. They suggested that Mn can embrittle PAGBs.

An unexpectedly high segregation level of Mn after 1 min of tempering at 450 °C (Fig. 6d shows Mn enrichment up to 11 at.% for this case), which is higher than estimated from an Mn diffusion length of 0.7 nm, and a surprisingly instantaneous embrittlement that appears after 10 s of tempering at 450 °C might be explained by either non-equilibrium segregation of Mn, occurring by either C–Mn complex [48] or vacancy–Mn pair formation, or by grain boundary relaxation [46]. Until now, there has been no confirmation of non-equilibrium segregation of Mn to martensitic (body-centered cubic, bcc) grain boundaries. For comparison, the alloy Mn9+B shows a substantially delayed embrittlement. The present observations suggest that Mn segregation is slowed down by non-equilibrium B segregation during cooling from the austenite regime. During tempering, B partially desegregates from PAGB and migrates to martensite lath and pocket boundaries, which is consistent with the observations of Hwang and Morris [9]. Once Mn segregates to PAGBs, B cannot compensate the embrittling effect caused by the Mn and the material fails along PAGBs. Nonetheless, the delay in temper embrittlement in the Mn9+B alloy at 450 °C can be utilized for welding applications during cooling in the heat-affected zone.

4.2. Austenite formation and its effect on impact toughness

During holding at a fixed temperature in a $\alpha+\gamma$ region, the decoration level of Mn at grain boundaries first increases, driven by equilibrium segregation and the formation of a new austenite phase [8,17], then decreases, as shown in Fig. 10. The decrease in Mn concentration is attributed to a formation of austenite or other phases that are rich in Mn. Such phase formation consumes the Mn from the grain boundaries, hence cleaning them from Mn segregation. Our results confirm the conclusions of Heo et al. [17] on Mn segregation in an Fe–12 at.% Mn alloy and suggest that this effect describes a general trend for all medium Mn steels [19]. In the Mn9 alloy, after 336 h of tempering at 450 °C, we observed an austenite zone with an Mn concentration up to 30 at.% (Fig. 8b). Nucleation of austenite requires an equality of chemical potentials between ferrite and austenite, which results in an oversaturation of Mn up to 36%. A detailed analysis of the Gibbs free energy for face-centered cubic (fcc) phase formation

Table 2. Grain boundary segregation values: absolute chemical concentration and excesses concentration for both the model alloys Mn9 and Mn9+B.

Alloy, treatment	Concentration (at.%)				Excess values Γ(atoms nm^{-2})			
	Mn	C	B	P	Mn	C	B	P
Mn9+B, quenched	8.3	1.1	2.4	0.01	0	1.20	2.8	0
Mn9, 450 °C, 1 min	12.1	0.7	–	0.01	4.80	1.10	–	0
Mn9+B, 450 °C, 10 min	11.0	1.2	0.7	0.06	2.40	1.24	1.26	0.09
Mn9+B, 450 °C, 1 h	16.5	0.4	0.5	0.2	5.10	1.10	0.60	0.20
Mn9, 450 °C, 48 h	18	1.6	–	0.65	9.80	0.60	–	0.50
Mn9, 450 °C, 336 h	8.0	0.7	–	0.50	4.98	1.12	–	0.55
Mn9, 600 °C,10 min	8.2	0.9	–	0.04	5.05	1.16	–	0

The values represent an averaged value of several experiments for the same tempering state.

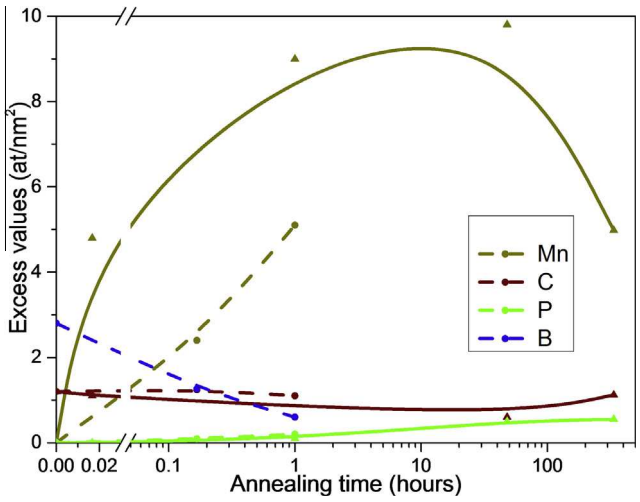

Fig. 10. Evolution of grain boundary excess values vs. tempering time at 450 °C for both alloys, Mn9 (solid line) and Mn9+B (dashed line).

in an Mn9 alloy is presented in Fig. 12. The growth of such a phase requires full thermodynamic equilibrium conditions that predict 25% Mn in austenite [49]. During growth, the Mn concentration equilibrates within austenite, hence the observed concentration of 30 at.% Mn in austenite (Fig. 8b) can be explained well by the incomplete homogenization of Mn inside the austenite in the early stage of the nucleation process. In contrast, P is rejected from the austenite and accumulates at the phase boundary, hence its concentration at the phase boundary is slightly increased. Besides the austenite, another Mn-rich phase is observed on some of the PAGBs after tempering at 450 °C, namely, a carbide with composition $M_{23}C_6$ (Fig. 11c and e). Opposed to the results of Heo et al. [17], no formation of α-Mn was detected in the current alloy Mn9.

Austenite formation accelerates with increasing temperature. A lower equilibrium concentration of Mn in austenite and a faster diffusion at 600 °C provide an increase in toughness after as little as 30 s of tempering through fast austenite nucleation at the grain boundaries. Fig. 11a and b show a small enrichment of Mn on the PAGB after 10 min of tempering at 600 °C – which is, however, below the nominal Mn concentration of 9 at.%.

The temperature dependence of the DBTT can also be explained in terms of the austenite formation kinetics. The experimental results show 18 at.% Mn enrichment after tempering for 48 h at 450 °C, which corresponds to an Mn diffusion length of 37 nm. A similar segregation level of Mn is expected for other tempering conditions with the same Mn diffusion length. From the temperature dependence of the Mn equilibrium concentration in austenite (Fig. 13), 18 at.% Mn corresponds to an austenite that is formed at

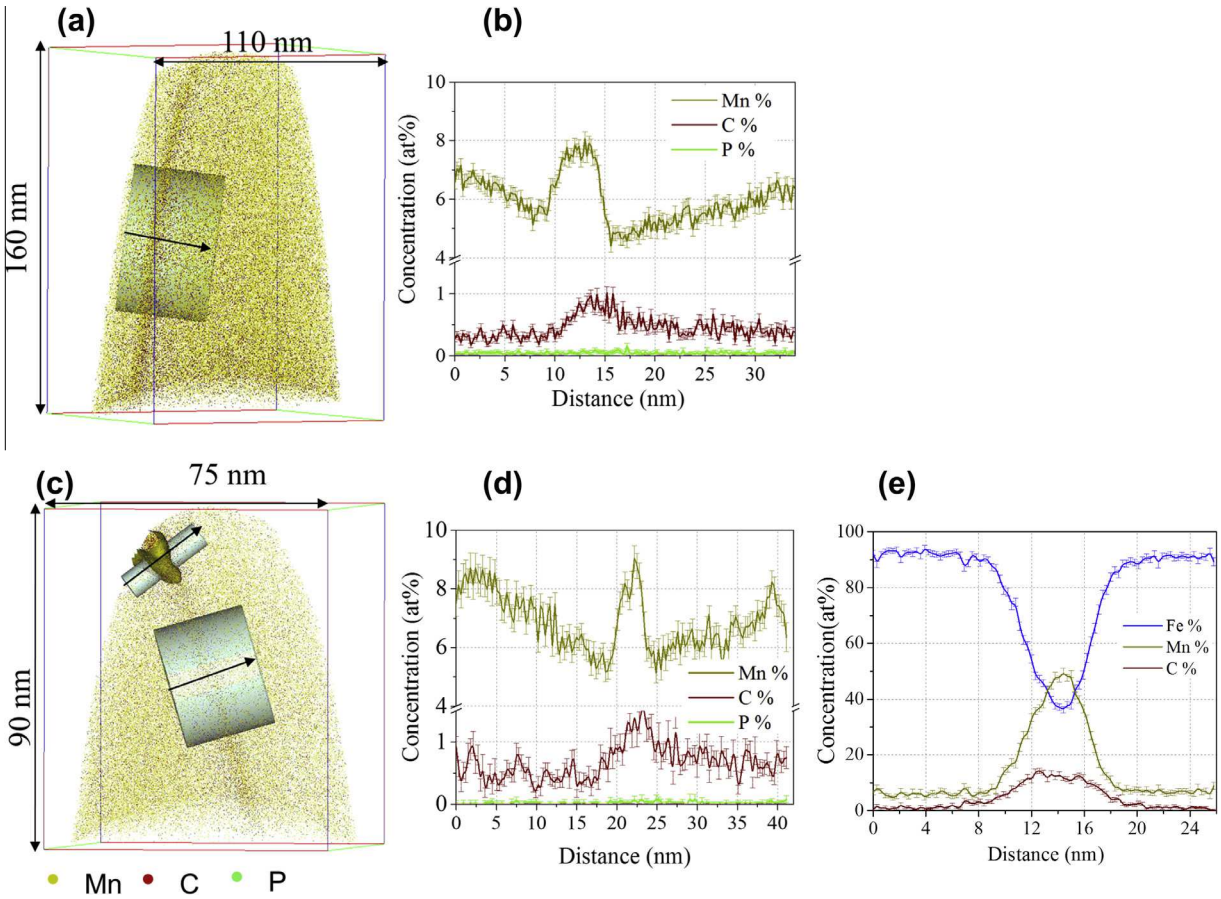

Fig. 11. (a) Ion distribution map of Mn9, tempered at 600 °C for 10 min, containing a PAGB; a corresponding 1-D concentration profile across the boundary is shown in (b); (c) ion distribution map of Mn9, tempered at 600 °C for 10 min followed by 450 °C 3 h; side view of a PAGB, containing a carbide particle: (d) 1-D concentration profile across PAGB; (e) 1-D concentration profile across a carbide particle, which is highlighted by an 18 at.% Mn iso-concentration surface.

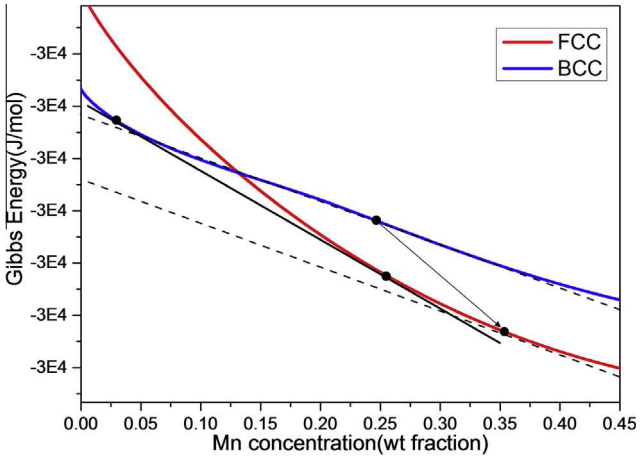

Fig. 12. ThermoCalc calculations of the Gibbs free energy for Mn9 at 450 °C for austenite (fcc) and ferrite (bcc) without the presence of a grain boundary. The nucleation of austenite requires equal chemical potentials of ferrite and austenite (parallel dotted lines). A tangent for the bcc curve at 25 at.% Mn should be parallel to a tangent that is plotted for the fcc phase. Plotting a parallel line results in a concentration of 36 wt.% Mn in fcc. A nucleus grows according to full equilibrium, with a concentration, obtained from plotting a tangent line between bcc and fcc, which results in 25.1 wt.% Mn in austenite and 3.7 wt.% Mn in ferrite.

540 °C. In region 1 in Fig. 13 the Mn equilibrium concentration in austenite exceeds 18 at.%; hence, austenite formation is unlikely. In region 2, in contrast, the Mn equilibrium concentration is lower than 18 at.% and formation of austenite is highly probable. When comparing this result with the impact toughness as a function of tempering temperature in Fig. 5, we observe a clear transition from the brittle-to-ductile fracture regime at a temperature around 540 °C. The ability to form austenite under a tempering condition defines the transition between brittle and ductile

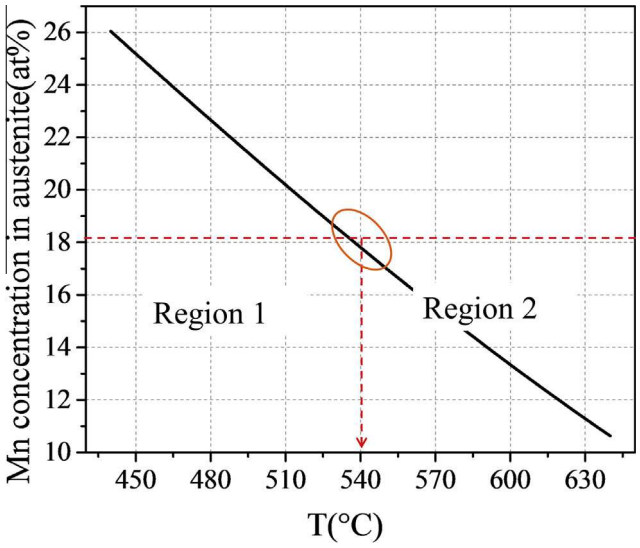

Fig. 13. Temperature dependence of the Mn equilibrium concentration in austenite. For all temperatures, an Mn concentration of 18 at.% is estimated at the grain boundary. In region 1, below 540 °C the Mn equilibrium concentration in austenite exceeds 18 at.% and austenite formation is unlikely. In region 2, the equilibrium concentration of Mn in austenite is below 18 at.% and austenite formation is expected.

regimes in the current alloy (Fig. 5). These results support the suggestion that the formation of austenite removes solute Mn from the grain boundaries, thus reducing the Mn-related embrittlement.

Besides its grain boundary cleaning effect, i.e., the removal of solute Mn from interfaces, the presence of austenite on grain boundaries is also assumed to play an important role in improving the impact toughness directly. This effect is attributed to a crack blunting or deflecting mechanism. Austenite may induce a TRIP effect and reduce crack propagation via local martensitic transformation [50,51]. For instance, through thermal cycling, the austenite fraction was increased in an Fe–5.5Ni alloy, which leads to an increase in the low-temperature impact toughness [52]. Besides the increased austenite volume fraction, its thermal and mechanical stability is also an important aspect affecting the impact toughness of the alloy [53].

4.3. Mechanisms of Mn embrittlement

The tempering of medium Mn alloys in the compositional range 5–12 at.% Mn [4,17,54] severely degrades toughness, and the segregation of Mn to grain boundaries is identified as a key reason. Several theories exist about the mechanism for this, as summarized by Heo et al. [17]. According to the pair-bonding approach by Seah [45], an enriched solute Mn content on a grain boundary leads to embrittlement as it decreases the sublimation enthalpy. Messmer and Briant [25] showed that a more electronegative metal in comparison to Fe – here Mn – attracts charges from the environment and thus weakens the metal–metal bonds in the grain boundary. Finally, it was suggested that larger atoms generally lead to grain boundary embrittlement [25].

Ab initio calculations of Olson et al. [47,55] on the Mn effect on the cohesion of a coherent Σ3 grain boundary have shown that Mn can directly decrease the grain boundary cohesion. Conducting calculations on a Σ11 grain boundary, Yang [46,56] came to similar conclusions, but pointed out that, on the one hand, as a solute, Mn can enhance grain boundary cohesion, though, on the other hand, the associated effect of the structural relaxation is detrimental to the overall cohesion of the grain boundary. Recently, Jin et al. [57] explained the embrittling effect of Mn in terms of a magnetic effect on the grain boundary. The magnetic moment of Mn, when segregated to the grain boundary, is anti-parallel to that of Fe, and hence causes a local volume change.

This brief review of possible Mn effects on grain boundary embrittlement supports our observations that Mn-decorated PAGBs can indeed undergo embrittlement after as little as 10 s of tempering. The fact that the embrittling effect occurs after such a short time suggests that structural relaxation, very fast diffusion and grain boundary decoration by Mn, associated with solute decohesion or a change in the magnetic contributions or their combinations, are the underlying mechanisms.

4.4. Methods of improving impact toughness

Grain refinement is an effective way to improve impact toughness [1,4,58–61]. A smaller grain size provides a lower level of individual grain boundary segregation [62,63]. Avoiding a temperature range where temper embrittlement

occurs or tempering at a higher temperature are other solutions for avoiding temper embrittlement. Alloying with 0.2 wt.% Mo failed to improve impact toughness in this work, but 2.5% Mo was shown to reduce the DBTT in Fe–8 wt.% Mn steel [8]. In the present work, microalloying with B decreased the DBTT and delayed temper embrittlement at 450 °C. B occupies grain boundary sites and reduces grain boundary energy, and is hence the driving force for Mn segregation. Desegregation of B from PAGBs in turn increases the driving force for Mn segregation, hence promoting grain boundary embrittlement.

Another important factor related to an improvement in impact toughness is the reversion of temper embrittlement after tempering at 450 °C. To study this problem closely, extra double-step heat treatments were performed for the alloy Mn9. The two heat treatment routes chosen here were 10 min at 450 °C followed by 10 min at 600 °C and 10 min at 600 °C followed by 10 min at 450 °C. Both treatments resulted in an improvement of impact toughness, i.e., the DBTT was reduced to −40 °C for both treatments. Even 30 s tempering at 600 °C prior to tempering at 450 °C is sufficient to improve the impact toughness and to change the brittle fracture mode from intercrystalline to transcrystalline. In a double-step heat treatment of 10 min at 600 °C plus further treatment at 450 °C, increasing the tempering time at 450 °C from 10 min to 24 h does not influence the DBTT. Analysis of Mn segregation performed by APT after such double-step heat treatments (shown in Fig. 11) shows no increase in Mn segregation compared to a single-step tempering for 10 min at 600 °C. In contrast, the Mn concentration observed on PAGBs was constantly increasing with tempering time during a single-step tempering at 450 °C. Thus, a positive effect of a double-step heat treatment on the resulting impact toughness can be understood in terms of the changing segregation behavior of Mn: tempering at 600 °C promotes nucleation of austenite, then, during the following tempering at 450 °C, Mn partitions into austenite or other Mn-rich phases, promoting its further growth. Thus, in the case of a combined 450 °C plus 600 °C treatment, the initial Mn grain boundary segregation at 450 °C transforms immediately to austenite at 600 °C, removing the embrittlement.

5. Summary

We studied the atomic scale mechanisms associated with Mn-dependent embrittlement in two medium Mn model steels, namely Mn9 and Mn9+B, at 450 and 600 °C. A delay in embrittlement in alloy Mn9+B is due to the non-equilibrium segregation of B to PAGBs, which decreases the grain boundary energy and reduces the diffusion of Mn to PAGBs. B desegregation during tempering in conjunction with promoted segregation of Mn causes an embrittling effect after longer holding times. An increase in impact toughness after longer tempering times is explained in terms of austenite reversion and the associated removal of solute Mn from the grain boundaries into the newly formed austenite. A double-step heat treatment (600 °C plus 450 °C) significantly improved the impact toughness by accelerating the austenite reversion kinetics at the higher temperature and changing the Mn segregation from grain boundaries into the austenite at the lower temperature.

The underlying embrittling mechanism of Mn was discussed and several possible reasons were identified, namely, a decrease in grain boundary cohesion by solute Mn and the influence of local magnetic contributions to grain boundary cohesion, causing a local volume change and internal stresses.

Acknowledgments

The authors gratefully acknowledge funding through the ERC Advanced Grant “SmartMet”.

References

[1] S. Jin, S.K. Hwang, J.W. Morris, J. Metall. Trans. A 6 (1975) 2.
[2] B.C. Edwards, M. Nasim, E.A. Wilson, Scr. Metall. 12 (1978) 377.
[3] S.K. Hwang, J.W. Morris, The Use of Microstructure Control to Toughen Ferritic Steels for Cryogenic Use. II Fe–Mn Steels. USSR-US Seminar on Applied Problems of Low-Temperature Materials and the Manufacture of Welded Cryogenic Structures, Kiev, USSR, October 12–14, 1976.
[4] M. Nikura, J.W. Morris, J. Metall. Trans. 11 (1980).
[5] G.A. Charushnikova, Y.E. Goldshtein, Y.G. Razumov, Metalloved. Term. Obrab. Met. 7 (1969) 33.
[6] J.D. Bolton, E.R. Petty, G.B. Allen, Metall. Trans. 2 (1970) 2915.
[7] M.J. Roberts, Metall. Trans. 1 (1970) 3287.
[8] M. Nasim, B.C. Edwards, E.A. Wilson, Mater. Sci. Eng. A Struct. Mater. 281 (2000) 56.
[9] S.K. Hwang, J.W. Morris, J. Metall. Trans. A 11A (1980) 1197.
[10] D. Duchateau, M. Guttmann, Met. Sci. 17 (1983) 229.
[11] J. Shi, J. Hu, C. Wang, C. Wang, H. Dong, W. Cao, J. Iron Steel Res. Int. 21 (2014) 208.
[12] A. Grajcar, R. Kuziak, W. Zalecki, Arch. Civ. Mech. Eng. 12 (2012) 334.
[13] H. Aydin, E. Essadiqi, I.-H. Jung, S. Yue, Mater. Sci. Eng. A Struct. Mater. 564 (2013) 501.
[14] D. Raabe, O. Dmitrieva, B. Sander, D. Ponge, Scr. Mater. 60 (2009) 1141.
[15] O. Dmitrieva, S.S.A. Gerstl, D. Ponge, D. Raabe, P. Choi, Ultramicroscopy 111 (2011) 623.
[16] F. Nikbakht, M. Nasim, C. Davies, E.A. Wilson, H. Adrian, Mater. Sci. Technol. 26 (2010) 552.
[17] N.H. Heo, Y.-U. Heo, S.-J. Kim, J.W. Nam, Acta Mater. 61 (2013) 4022.
[18] K.H. Kwon, I.-C. Yi, Y. Ha, K.-K. Um, J.-K. Choi, K. Ohishic, N.J. Kim, Scr. Mater. 69 (2013) 420.
[19] D. Raabe, M. Herbig, S. Sandlöbes, Y. Li, D. Tytko, M. Kuzmina, D. Ponge, P.-P. Choi, Curr. Opin. Solid State Mater. Sci. 18 (2014) 1.
[20] P.J. Felfer, B. Gault, G. Sha, L. Stephenson, S.P. Ringer, J.M. Cairney, Microsc. Microanal. 18 (2012) 359.
[21] M.K. Miller, R.G. Forbes, Mater. Charact. 60 (2009) 461.
[22] T.F. Kelly, M.K. Miller, Rev. Sci. Instrum. 78 (2007).
[23] S. Song, R.G. Faulkner, P.E.J. Flewitt, J. Mater. Sci. 34 (1999) 5549–5556.
[24] Y. Nie, W. Hui, W. Fu, Y. Weng, J. Iron Steel Res. Int. 14 (2007) 53.
[25] R.P. Messmer, C.L. Briant, Acta Metall. 30 (1982) 457.
[26] B.P. Geiser, D.J. Larson, E. Oltman, S. Gerstl, D. Reinhard, T.F. Kelly, T.J. Prosa, Microsc. Microanal. 15 (2009) 292.
[27] E. Hornbogen, H. Kreye, J. Mater. Sci. 17 (1982) 979.
[28] M.A. Kuzmina, M. Herbig, D. Ponge, C. Borchers, B. Gault, D. Raabe, in preparation.
[29] J. Morris, J. William, ISIJ Int. 51 (2011) 1569.
[30] B. Hwang, T.-H. Lee, S.-J. Park, C.-S. Oh, S.-J. Kim, Mater. Sci. Eng. A Struct. Mater. 528 (2011) 7257.
[31] M. Lambrecht, L. Malerba, A. Almazouzi, J. Nucl. Mater. 378 (2008) 282.

[32] H. Kwon, Metall. Trans. A 22A (1991) 1119.
[33] P. Lejček, S. Hofmann, V. Paidar, Acta Mater. 51 (2003) 3951.
[34] M.K. Miller, L. Yao, Curr. Opin. Solid State Mater. Sci. 17 (2013) 203.
[35] B.W. Krakauer, D.N. Seidman, Phys. Rev. B 48 (1993) 6724.
[36] M. Herbig, D. Raabe, Y.J. Li, P. Choi, S. Zaefferer, S. Goto, Phys. Rev. Lett. 112 (2014) 126103.
[37] D. Raabe, S. Sandlöbes, J. Millán, D. Ponge, H. Assadi, M. Herbig, P.-P. Choi, Acta Mater. 61 (2013) 6132.
[38] O. Dmitrieva, G. Inden, J. Millán, P. Choi, J. Sietsma, D. Raabe, D. Ponge, Acta Mater. 59 (2011) 364.
[39] L. Yuan, D. Ponge, J. Wittig, P. Choi, J.A. Jiménez, D. Raabe, Acta Mater. 60 (2012) 2790.
[40] N. Nakada, R. Fukagawa, T. Tsuchiyama, S. Takaki, D. Ponge, D. Raabe, ISIJ Int. 53 (2013) 1286.
[41] N. Nakada, T. Tsuchiyama, S. Takaki, D. Ponge, D. Raabe, ISIJ Int. 53 (2013) 2275.
[42] Y.J. Li, P. Choi, C. Borchers, S. Westerkamp, S. Goto, D. Raabe, R. Kirchheim, Acta Mater. 59 (2011) 3965.
[43] Y. Li, D. Raabe, M. Herbig, P.-P. Choi, S. Goto, A. Kostka, H. Yarita, C. Borchers, R. Kirchheim, Phys. Rev. Lett. 113 (2014) 106104.
[44] R. Wu, A. Freeman, G. Olson, Phys. Rev. B Condens. Matter Mater. Phys. 53 (1996) 7504.
[45] M.P. Seah, Acta Metall. 28 (1979) 955.
[46] R. Yang, D.L. Zhao, Y.M. Wang, S.Q. Wang, H.Q. Ye, C.Y. Wang, Acta Mater. 49 (2001) 1079.
[47] W. Geng, A.J. Freeman, G.B. Olson, Phys. Rev. B 63 (2001) 165415.
[48] Y.N. Dastur, W.C. Leslie, Metall. Trans. A 12A (1981) 749.
[49] Thermo-Calc Software AB. TCFE7_TCS steels/Fe-Alloys Database, Version 7.1, Thermo-Calc Software AB, Stockholm, n.d.
[50] M.-M. Wang, C.C. Tasan, D. Ponge, A. Kostka, D. Raabe, Acta Mater. 79 (2014) 268.
[51] Z. Mei, J.W. Morris, J. Metall. Trans. A 21 (1990) 3137.
[52] J.I. Kim, C.K. Syn, J.W. Morris, Metall. Trans. A 14 (1983) 93.
[53] C.G. Lee, S.-J. Kim, T.-H. Lee, S. Lee, Mater. Sci. Eng. A Struct. Mater. 371 (2004) 16.
[54] H.J. Lee, The Study of Intergranular Embrittlement in Fe–12Mn Alloys (PhD thesis), University of California, Berkeley, 1982.
[55] L. Zhong, R. Wu, A.J. Freeman, G.B. Olson, Phys. Rev. B 55 (1997) 11133.
[56] R. Yang, Y.M. Wang, R.Z. Huang, H.Q. Ye, C.Y. Wang, Phys. Rev. B 65 (2002) 94112.
[57] H. Jin, I. Elfimov, M. Militzer, J. Appl. Phys. 115 (2014).
[58] R. Song, D. Ponge, D. Raabe, J.G. Speer, D.K. Matlock, Mater. Sci. Eng. A Struct. Mater. 441 (2006) 1.
[59] R. Song, D. Ponge, D. Raabe, R. Kaspar, Acta Mater. 53 (2005) 845.
[60] M. Calcagnotto, D. Ponge, D. Raabe, Mater. Sci. Eng. A Struct. Mater. 527 (2010) 7832.
[61] X. Sun, Z. Li, Q. Yong, Z. Yang, H. Dong, Y. Weng, Sci. China Technol. Sci. 55 (2012) 1797.
[62] K. Ishida, J. Alloys Compd. 235 (1996) 244.
[63] M. Calcagnotto, D. Ponge, D. Raabe, Metall. Mater. Trans. A 43 (2011) 37.